Supporting Information: Electrochemically induced changes in TiO$_2$ and carbon films, studied with QCM-D

Aditya Narayanan, Frieder Mugele, Michael H.G. Duits*

Physics of Complex Fluids group, MESA$^+$ Institute, University of Twente

PO Box 217, 7500 AE Enschede, The Netherlands

*email: m.h.g.duits@utwente.nl

1 Accuracy and robustness of the viscoelastic modeling.

In this section we present some details of the model fitting, especially in relation to the viscoelastic exponents. We examine the TiO$_2$ sample to check the modelling, and show some results for other systems later in the SI. Here, we point out an inherent limitation of the eQCM-D for studying SEI. The solid liquid interface is quite complex in Lithium batteries and is frequently comprised of multiple layers. Lithium intercalates into the outer material, thereby modifying it while an inner inorganic and outer organic SEI layer forms at the interface[1-2]. Additionally, these layers can vary spatially in homogeneity and porosity. While the acoustic shear waves of the QCM are sensitive to these factors, the reliance on a model makes these factors difficult to elucidate. This is further complicated by the fact that neither the structure nor the physical properties of the layer are known *a priori*. In this section, in addition to exploring the robustness of our fits, we also explore the contributions these effects have on our system.

1.1 Third order Perturbation Analysis

$$\frac{\Delta \tilde{f}}{f_0} \approx \frac{-2nf_0 m_f}{Z_q}\left[1 - 2\pi i n \frac{\tilde{J}_f(\omega)}{\rho_f} f_0 \rho_l \eta_l\right] \qquad (S1)$$

The derivation of Equation S1 (Equation 3 in the main text) relies on the Small Load Approximation (SLA), which strictly applies only when layers are thin, and shifts are small.

$$\frac{\Delta \tilde{f}}{f_0} \approx \frac{-2nf_0 m_f}{Z_q}\left[1 - 2\pi i n \frac{\tilde{J}_f(\omega)}{\rho_f} f_0 \rho_l \eta_l + (1+i)\sqrt{\frac{f_0 \rho_l \eta_l}{n\pi Z_q^2}} + i\frac{2\pi f_0 n \rho_l \eta_l}{Z_q^2}\right] \qquad (S2)$$

To cover for the regimes with thick SEI formation, we use a modified version of equation 3 / S1 for our fitting. The third order perturbation equation[2] (S2) contains (small) correction terms that avoid errors in the SLA due to large shifts. These errors usually show up in the n-dependence of $\tilde{J}_f(\omega)$. For our experimental data, we only see small differences in the model outputs of the two approaches. The third order perturbation equation mainly improves the fits for the half band-width shifts.

## 1.2 Quality of overall fit, as a function of viscoelastic exponents

We first focus on the effect of the viscoelastic exponents on the goodness of fit; the Root Mean Squared Error (RMSE):

$$RMSE = \sqrt{\frac{1}{n}\sum_n (x_{modeled} - x_{experimental})^2}$$

Where x is the frequency or half-bandwidth shift and the summation is over the whole experiment for overtones 5 through 13. Fig. S1 shows maps of the RMSE of the frequency shift, bandwidth shift and the combination. During fitting, it is the RMSE of the combination that is minimized. As predicted by Equation 3 / S1, the RMSE of the frequency shift is most dependent on β'' and that of the half-bandwidth shift on β'. The overall RMSE shows a shallow minimum, implying that the choices of β' and β'' are not extremely critical (within a small range) to the fits. At the minimum, the RMSE is below 20Hz which for our system at overtone 5 corresponds to a Sauerbrey mass of 6.5×10^{-7} kgm^{-2} (i.e. well below the found masses of O (10^{-5} kgm^{-2}). For the other overtones, the fitting error is similar.
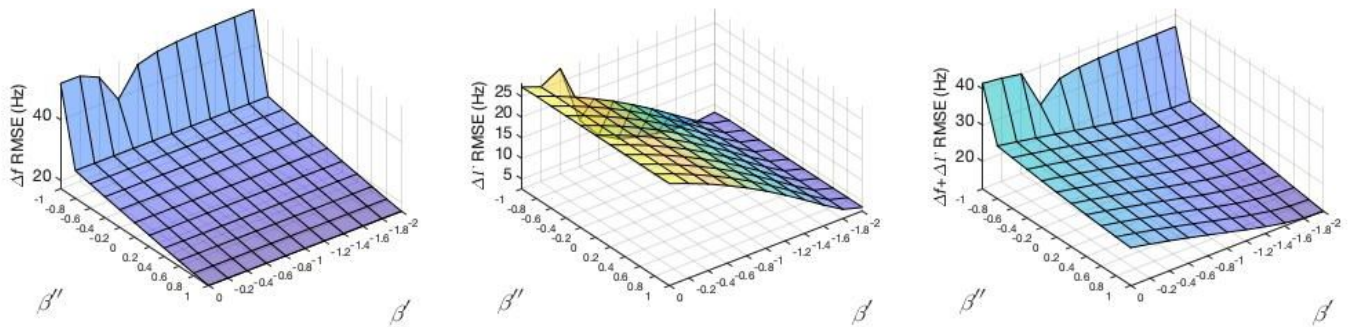
Fig S1. *Maps of the Root Mean Squared Error (RMSE) for the grid-fit of the QCM data for TiO$_2$ (all cycles in Fig. 2 of main text), allowing the exponents β' and β'' to vary independently within their physical bounds. **Left:** frequency, **Center:** half bandwidth shift and **Right:** combination*
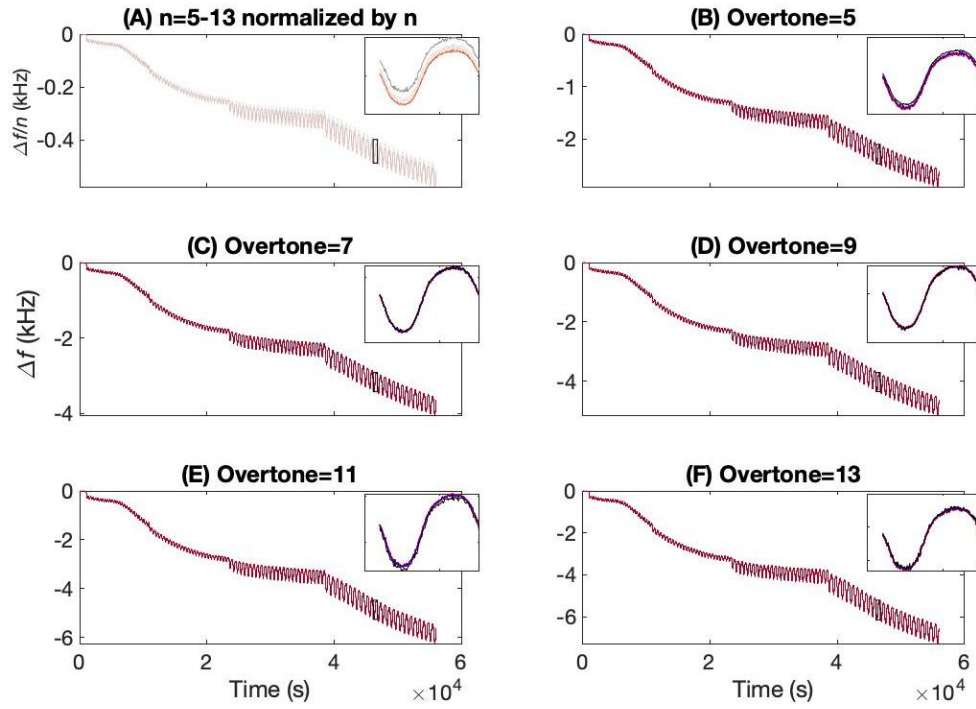
Fig S2. (A) *Experimental frequency shifts normalized by overtone number.* ***(B-F)*** *Experimental frequency shift (black) and closest modeled shift (blue) and shifts for 24 nearby combinations of the viscoelastic exponents (red) for each overtone. Inset is a zoom of the boxed region.*
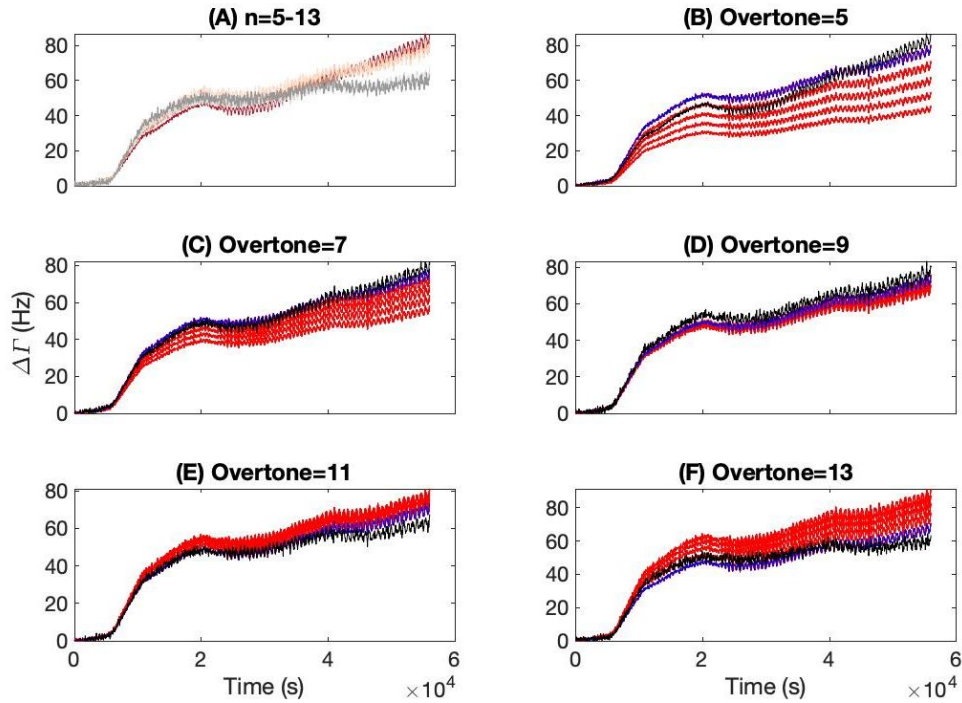
Fig S3. (A) *Experimental half bandwidth shifts for all overtones.* ***(B-F)*** *Half bandwidth shifts per overtone from experiments (black), best model fit (blue) and 24 nearby combinations of the viscoelastic exponents (red).*

We now examine 25 model fits from the variation of the combination of β' and β'' around the best one. From the best combination, each exponent was varied in steps of 0.2 for a total range of 0.8 (40% of total range) within the bounding values. Figures S2 and S3 show the experimental and modelled frequency- and half-bandwidth- shifts for these combinations. From Fig. S2A it is clear that there is a non-zero viscoelastic compliance, as the normalized frequency-shift curves do not superimpose. Fig. S3A shows that the half-bandwidth shifts almost superimpose, which implies that the layer's elastic compliance is nearly proportional to n^{-2}. This is consistent with the best fits being found for $\beta' = -2$ and $\beta'' = 1$.

Fig. S2 also shows that for a reasonable range of the exponents, there is almost no visible difference in the modelled frequency-shifts. This implies that the viscous compliance makes only a minor contribution to the frequency shift. As a consequence, the fitted layer mass should be largely decoupled from the fitted compliance and depend mainly on the frequency shift (approaching the Sauerbrey result: as $\tilde{J} \rightarrow 0$, the second term in the bracket of equation 3 / S1 goes to zero).

While the RMSE values for the frequency and half bandwidth shift are similar, the differences in the modelled half-bandwidth curves for different exponents are larger. This is due to the proportional dependence of the half bandwidth shifts on the elastic compliance.

1.3 Fitted mass and compliances as a function of visco-elastic exponents

To examine the uncertainties in the fit parameters (i.e. m_f, J'_{ref} and J''_{ref}), we calculate the Root Mean Squared Difference (RMSD):

$$RMSD = \sqrt{\frac{1}{n}\sum_n (x_{\beta' \beta''} - x_{best \, \beta' \, \beta''})^2}$$

Where x is the parameter for the choice of β' and β'' and the summation is over the whole experiment (as before). The RMSD shows us how far a predicted curve for a set of β' and β'' is from the curve predicted for the lowest RMSE. Figure S4 shows maps of the logarithm of the RMSD for m_f, J'_{ref} and J''_{ref}. As expected from the form of Equation 3 / S1, the m_f and J''_{ref} RMSD depend mainly on β'' and the J''_{ref} RMSD on β'. The low values of the m_f RMSD around the best fit compared to the mean m_f throughout the experiment again confirm that m_f is rather insensitive to the choice of the exponents.
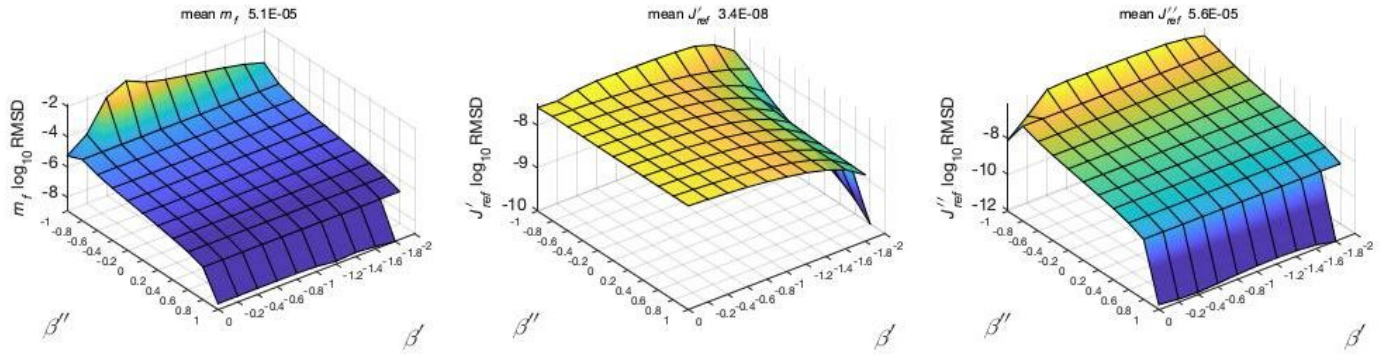
Fig S4. *Maps of the logarithm of the Root Mean Squared Difference (RMSD) for* **Left:** m_f, **Center:** J'' *and* **Right:** J' *fitted over the whole experiment, as a function of the exponents β' and β''. Regions with a RMSD below 1% of the mean of the variable are in dark blue. For J' and J'' the first 1000s are excluded from the RMSD calculation due to the small layer thickness and hence high uncertainty.*

While the RMSD provides a good measure of how sensitively an extracted fit parameter depends on chosen constraints (i.e. the values taken for β' and β''), it does not show how this 'error' manifests in the time-dependent functions. In Fig. S5 we examine the outputs of m_f, J'_{ref} and J''_{ref} for different combinations of the exponents around the best choice. There is a negligible difference in the different m_f curves, again indicating that the fitted value of m_f should be accurate, given reasonable choices for the viscoelastic exponents. The J'_{ref} and J''_{ref} curves on the other hand are visibly different. However, the different exponent choices just offset the curves. Thus, while their absolute values may be inaccurate, the trends in their values over the experiment should be reliable.
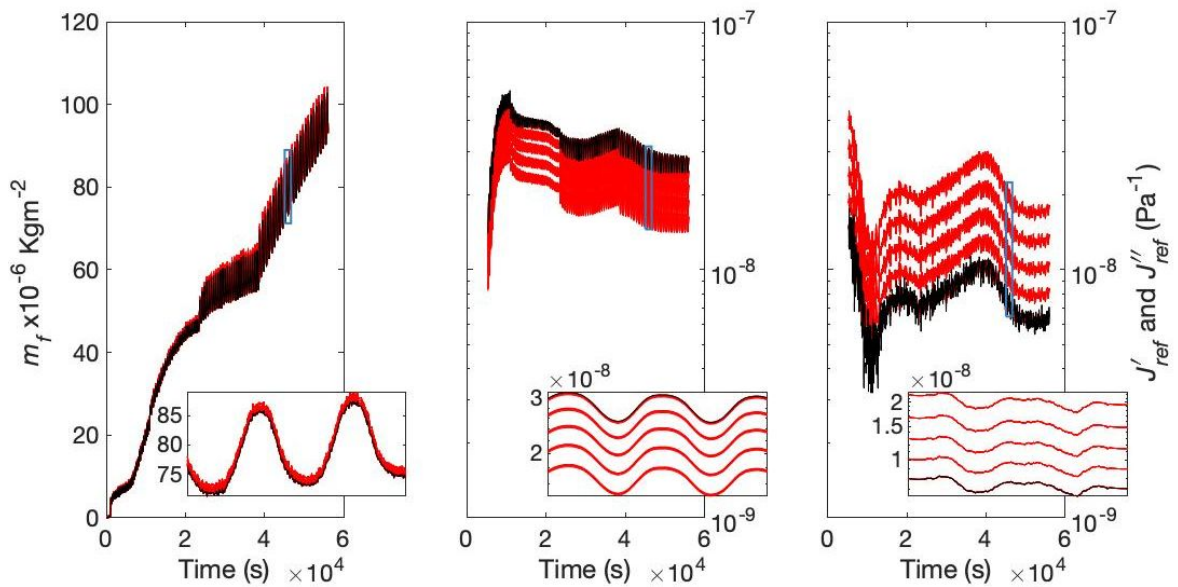

Fig S5. *Extracted fit parameters* **(A)** m_f, **(B)** J''_{ref} *and* **(A)** J'_{ref} *for the best (black) and 24 next best (red) combinations of the viscoelastic exponents. Insets are a zoom of the boxed region. J''_{ref} and J'_{ref} curves have been Savitz-Golay smoothed to aid visibility.*

1.4 Fitted mass and compliances as a function of estimated layer density

We now consider the effect of the estimated layer density on the modelling results in Fig. S6. We performed the fitting for layer densities from 1000 to 2000 Kgm^{-3}. Similar to the effect of the exponents, there is no effect of the layer density on m_f, while the J'_{ref} and J''_{ref} curves are offset.
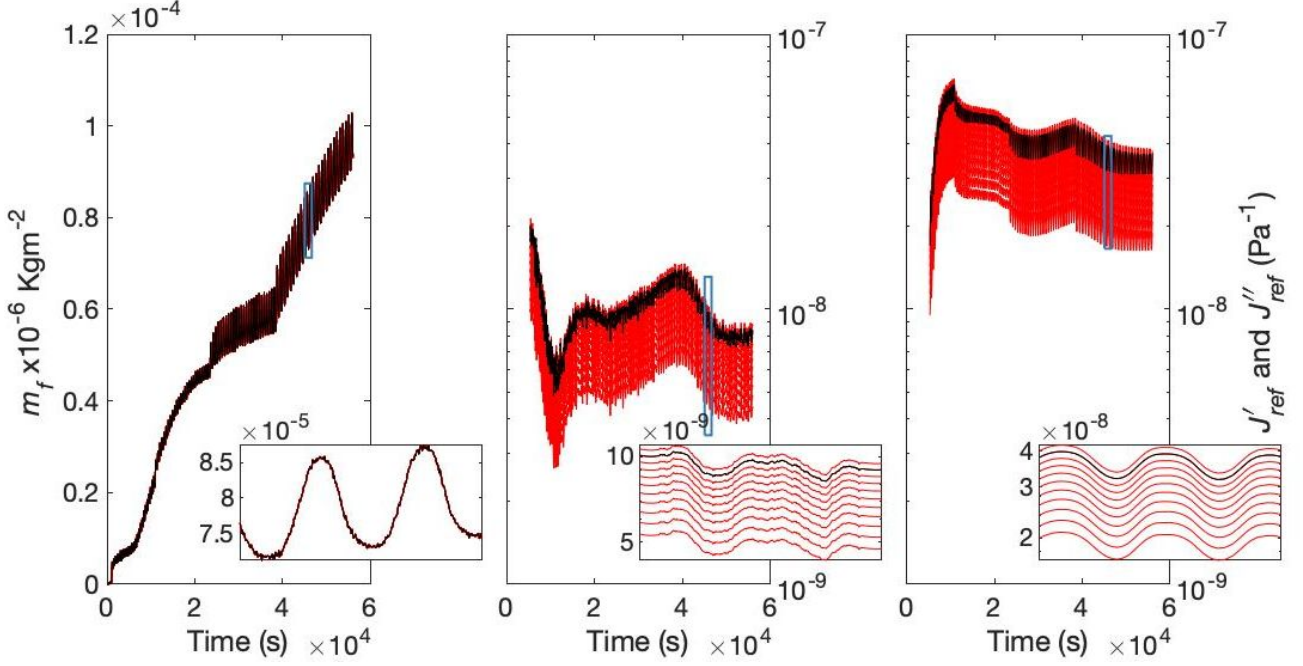
Fig S6. *Model outputs (A) m_f, (B) J''_{ref} and (A) J'_{ref} for eleven different layer densities (1000-2000 kgm^{-3}). Insets are a zoom of the boxed region. J''_{ref} and J'_{ref} curves have been SG smoothed to aid visibility.*

1.5 Effect of multilayers

From the small load approximation, for a layer that has a compliance that varies with the thickness z, viz. a multilayer, if the densities are very close ($\rho_l \approx \rho_f$) and the layer is thin[2],

$$\frac{\Delta \tilde{f}}{f_0} \approx \frac{-2n\,\rho_l f_0}{Z_q} \int_0^{z_{tot}} [1 - i2\pi f_0 \eta_l \tilde{J}_f(\omega,z)]dz$$

From this equation, it is clear for a small viscous compliance (~10^{-8} Pa^{-1}), the real part of the second term is small (order 10^{-4}) and thus the effect of a multilayer structure on the predicted mass is very small. There will however be an effect on the predicted, now z-dependant, elastic compliance. Without prior knowledge on the actual multilayer structure, it is not possible to qualify this effect and the predicted compliance becomes an 'apparent compliance' for the multilayer as a whole.

1.6 Effect of roughness

The roughness found for typical SEI layers has a lateral scale l_r much smaller than the shear wave penetration depth δ. For a roughness of height h_r, assuming a rigid layer[2],

$$\frac{\Delta\tilde{f}}{f_0} \approx \frac{-1}{\pi Z_q}\sqrt{\pi f_0 \rho_l \eta_l}[(1+i) + 3\sqrt{\pi}\frac{h_r^2}{l_r\delta} + 2(i-1)\frac{h_r^2}{\delta^2}]$$

The case $h_r = 0$ corresponds to the bare crystal in liquid. For SEI, h_r is of the order of a few nm, δ close to 1000nm and l_r a few tens of nanometers. Thus, the second two terms in the bracket are quite small leading to frequency shifts of a few to a few tens of Hertz and a bandwidth shift below 1 Hertz. This is well below the fitting error of the experiment and thus not expected to play a role.

2 Other Graphs

2.1 Raman Spectroscopy of Sputtered Carbon

The sputtered Carbon layer as used in the eQCM-D experiments was mimicked by DC magnetron sputtering Carbon on a Si wafer using a graphite (99.999%) target disk in an Argon plasma at a pressure of 6.6 μbar (as in Section 2.2).

Raman measurements were done with a WiTec alpha 300R Raman microscope connected to a 532 nm laser. A 600 g/mm grating was used, providing a spectral resolution of around 2.3 cm^{-1}. For high spatial resolution, a 100× objective (Zeiss EC "Epiplan-Neofluar" DIC, Numerical Aperture (NA) = 0.9) was chosen. Laser power at the sample was measured using an optical power meter (Thorlabs) and was kept at 20 mW. Raman mapping was performed by raster scanning across a 50 x 50 μm^2 region at a resolution of 100 x 100 pixels. For clarity, the notation I(D) and I(G) refer to the peak intensity values of the D and G band, observed in the Raman spectrum of the carbon coating at 1350 cm^{-1} and 1542 cm^{-1} respectively.
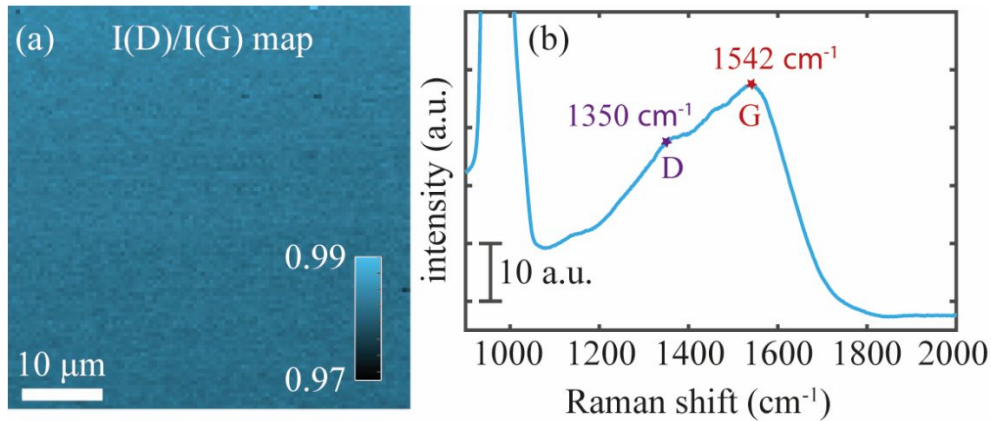

Fig S7 : (a) I(D)/I(G) ratio map of a 50 x 50 μm^2 region showing uniform distribution of the amorphous nature of the carbon coating. (b) Mean Raman spectrum of the same region as in

(a), showing a broad D and G band at 1350 cm^{-1} and 1542 cm^{-1} respectively, characteristic of amorphous carbon.

Raman spectroscopy is a versatile tool for determination of the crystallinity of carbonaceous materials. By monitoring the peak position of the G band and the I(D)/I(G) ratio, one could comment on the crystallinity of the substrate.[3] Comparing the values with literature (refer stage 2 in Fig. 4 of ref. [3]), we find that the I(D)/I(G) ratio (~0.98), as shown in Fig. S7a, and the G band position (1542 cm^{-1}) as shown in the mean Raman spectrum of the coating in Fig. S7b, are close to the values characteristic of amorphous carbon. Crystalline domains could alter the I(D)/I(G) ratio and G peak position considerably. By mapping the I(D)/I(G) ratio over a certain region (Fig. S7a), we can conclude that the amorphous nature of the coating is uniform, with the ratio varying only between 0.97 and 0.99 over a 50 x 50 μm^2 region.

2.2 X-ray Reflectivity and Diffraction on Sputtered Carbon

The same sputtered layer was also studied with X-ray reflectivity and diffraction. Measurements were done using a Bruker D8 Discover X-ray diffractometer with a rotating anode microfocus X-ray source (TXS) combined with a focusing mirror (Montel). Cu-Kα radiation was used to illuminate the sample.
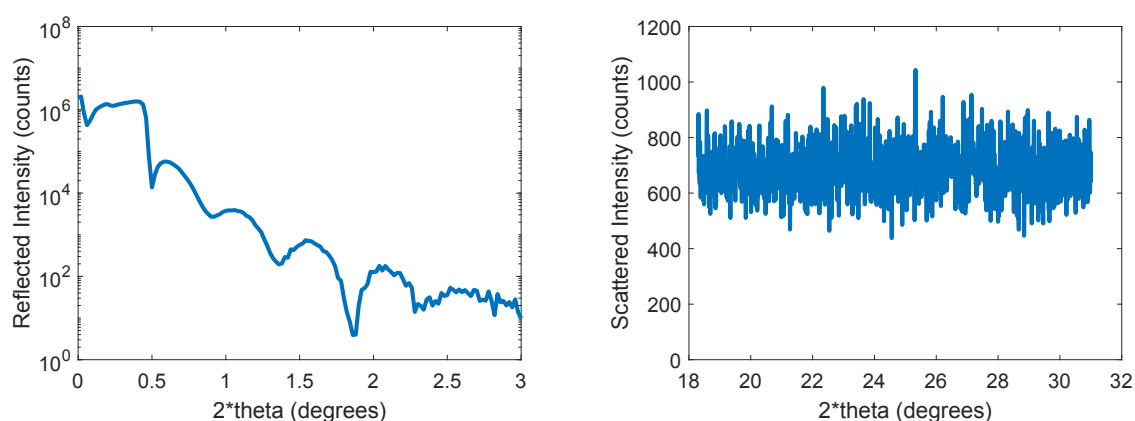
***Fig S8. Left:*** *X-ray reflectivity versus 2Θ (Θ=incident angle). The periodic pattern for 2Θ > 0.5 degrees indicates the presence of a ~17 nm thick (Carbon) layer.* ***Right:*** *X-ray diffractogram, for 2Θ =21-33 degrees. Absence of the typical (002) reflection at 25.5 degrees indicates that the Carbon layer is amorphous.*

To confirm the presence of the Carbon layer, an X-ray reflectivity measurement was done. The resulting spectrum in Fig. S8 (left) confirms the presence of a layer with a thickness that is in good accordance with the sputtering time. The angle dependent scattered intensity showed a very gradually decreasing intensity, without showing even the strongest characteristic (002) crystalline peak of graphite (expected at *2Θ* ~25.5 degrees for Cu-Kα radiation[4-5]); see Fig. S8 (right) for a broad angular range around this peak. This confirms that the Carbon layer is amorphous.
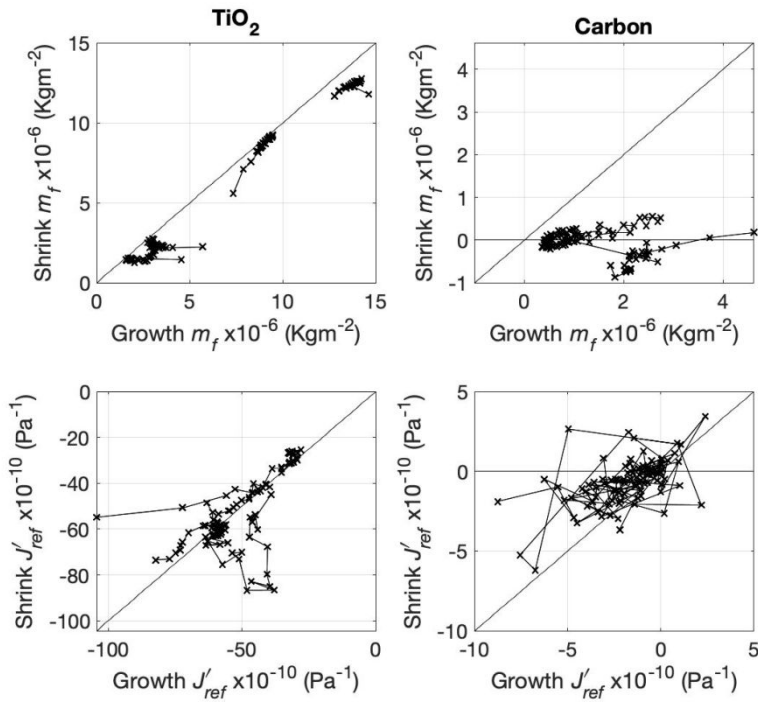
2.3 Cyclic Voltammetry
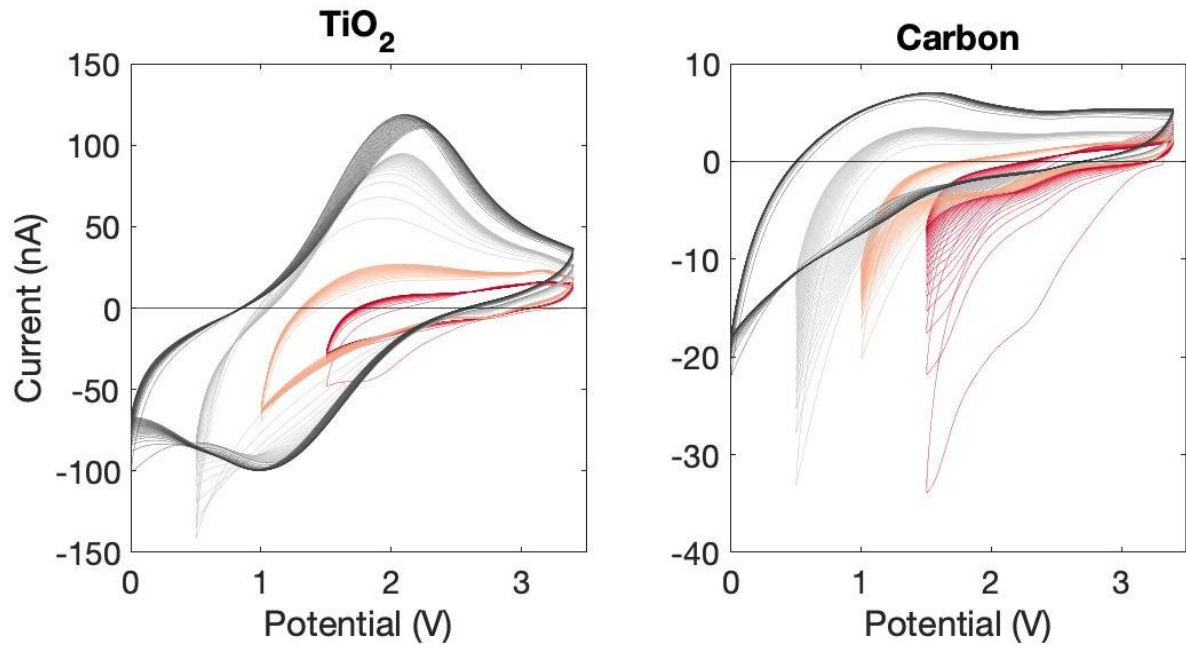
Fig S9. *Cyclic Voltammograms for **Left:** TiO$_2$ and **Right:** Carbon for the experiment in Figure 2 (main text).The voltage windows are 3.4V to Red: 1.5V Teal: 1V Gray: 0.5V and Black:0V.*

2.4 Correlations between mass and elastic compliance in growth and shrink stages

Fig S10. *Correlation plots for the shrinkage and growth of m_f and J'_{ref} for TiO$_2$ and Carbon within the same charge-discharge cycle, based on Fig. 7. The black line represents a 1:1 correlation. For J'_{ref} the first 4 cycles have been omitted.*

References

1. Kim, S.-P.; Van Duin, A. C.; Shenoy, V. B., Effect of electrolytes on the structure and evolution of the solid electrolyte interphase (SEI) in Li-ion batteries: A molecular dynamics study. *Journal of Power Sources* **2011,** *196* (20), 8590-8597.
2. Johannsmann, D., The quartz crystal microbalance in soft matter research. *Fundamentals and modeling. Switzerland: Springer International Publishing* **2015**.
3. Ferrari, A. C.; Robertson, J., Raman spectroscopy of amorphous, nanostructured, diamond–like carbon, and nanodiamond. *Philosophical Transactions of the Royal Society of London. Series A: Mathematical, Physical and Engineering Sciences* **2004,** *362* (1824), 2477-2512.
4. Franklin, R. E., the interpretation of diffuse x-ray diagrams of carbon. *Acta Crystallographica* **1950,** *3* (2), 107-121.
5. Li, Z. Q.; Lu, C. J.; Xia, Z. P.; Zhou, Y.; Luo, Z., X-ray diffraction patterns of graphite and turbostratic carbon. *Carbon* **2007,** *45* (8), 1686-1695.